Dominant Patterns of Summer Ozone Pollution in Eastern China and Associated Atmospheric Circulations

Zhicong Yin [1,2], Bufan Cao[1], Huijun Wang[1,2]

[1]Key Laboratory of Meteorological Disaster, Ministry of Education / Joint International Research Laboratory of Climate and Environment Change (ILCEC) / Collaborative Innovation Center on Forecast and Evaluation of Meteorological Disasters (CIC-FEMD), Nanjing University of Information Science & Technology, Nanjing 210044, China

[2]Nansen-Zhu International Research Centre, Institute of Atmospheric Physics, Chinese Academy of Sciences, Beijing, China

Correspondence to: Zhicong Yin (yinzhc@163.com)

Abstract. Surface ozone has been severe during summers in the eastern parts of China, damaging human's health and flora and fauna. During 2015–2018, ground-level ozone pollution increased and intensified from south to north. In North China and Huanghuai region, the O_3 concentrations were highest. Two dominant patterns of summer ozone pollution were determined, i.e., a south-north covariant pattern and a south-north differential pattern. The anomalous atmospheric circulations composited for the first pattern manifested as a zonally enhanced East Asia deep trough and as a west Pacific subtropical high whose western ridge point shifted northward. The local hot, dry air and intense solar radiation enhanced the photochemical reactions to elevate the O_3 pollution levels in North China and Huanghuai region, however the removal of pollutants were decreased. For the second pattern, the broad positive geopotential height anomalies at high latitudes significantly weakened cold air advection from the north, and those extending to North China resulted in locally high temperature near the surface. In a different manner, the west Pacific subtropical high transported sufficient water vapor to the Yangtze River Delta and resulted in locally adverse environment for the formation of surface ozone. In addition, the most dominant pattern in 2017 and 2018 was different from that in previous years, which is investigated as a new feature.

1. Introduction

High levels of ozone occurs both in the stratosphere and at the ground level. Stratospheric ozone forms a protective layer that shields us from the sun's harmful ultraviolet radiation. However, surface ozone is an air pollutant and has harmful effects on people and on the environment, such as damaging human lungs (Day et al., 2017) and destroying agricultural crops and forest vegetation (Yue et al., 2017). Worldwide, polluted ozone events are more frequent and stronger in China than those that have taken place in Japan, South Korea, Europe, and the United States (Lu et al., 2018). Due to their close relationship with anthropogenic emissions (Li et al., 2018), the high O_3 concentrations in China are mainly observed in urban regions, such as in North China (NC, Figure 1b), the Yangtze River Delta (YRD) and the Pearl River Delta (PRD) where rapid development has occurred in recent decades (Wang et al., 2017). An increase in surface ozone levels was found in China in 2016 and 2017 relative to 2013 and 2014 (Lu et al., 2018). The O_3 pollution levels in Beijing-Tianjin-Hebei (part of NC) were the most severe in China (Wang et al., 2006; Shi et al., 2015) and this situation has been getting worse. The O_3 concentrations in North China underwent a significant increase in the period of 2005–2015, with an average rate of 1.13 ± 0.01 ppbv yr^{-1} (Ma et al., 2016). Although far away from the anthropogenic emissions, the summer (June-July-August, JJA) O_3 on the highest mountain over NC (Mount Tai) increased significantly by 2.1 ppbv yr^{-1} from 2003 to 2015 (Sun et al., 2016). The O_3 levels generally presented increasing trends from 2012 to 2015 in the YRD (Tong et al., 2017), e.g., the O_3 concentrations in Shanghai (a mega-city) increased by 67% from 2006 to 2015 (Gao et al., 2017). In the PRD region, O_3 increased by 0.86 ppbv yr^{-1} from 2006 to 2011 (Li et al., 2014). Furthermore, ozone pollution is projected to increase in the future over eastern China (Wang et al., 2013).

Although deep stratospheric intrusions may elevate surface ozone levels (Lin et al., 2015), the main source of surface ozone is the photochemical reactions between the oxides of nitrogen (NO_x) and volatile organic compounds (VOC), i.e., NO_x + VOC = O_3. The concentrations of NO_x and VOC are fundamental drivers impacting ozone production, and are sensitive to the regime of ozone formation, i.e., NO_x-limited or VOC-limited (Jin and Holloway 2015). The changes in fine particulate matter are also a pervasive factor for the variation in ozone concentration. Employed the GEOS-Chem chemical transport model, Li et al. (2018) found that rapid decreases in fine particulate matter levels significantly stimulated ozone production in NC by slowing down the aerosol sink of hydro-peroxy radicals. In addition, the meteorological conditions also influenced the ozone levels via modulation of the photochemical episodes and removal effects (Yin et al., 2019; Lu et al., 2019). Intense solar radiation accelerated chemical O_3 production (Tong et al., 2017). A severe heat wave in the YRD contributed to high O_3 concentrations in 2013 (Pu et al., 2017). Winds had an impact on the O_3 and its precursors at downwind locations (Doherty et al., 2013). Local meteorological influences are always related to specific large-scale atmospheric circulations. The changes in the East Asian summer monsoon led to 2–5% interannual variations in surface O_3 concentrations over central eastern China (Yang et al., 2014). Continental anticyclones created sunny and calm weather, which are favourable conditions for O_3 production in NC (Ding et al., 2013; Yin et al., 2019). Due to the associated transports of pollution from inland, tropical cyclones are often related to the evaluation of surface O_3 levels in the coastal areas of PRD (Ding et al., 2004). Basing on a case study in 2014, further studies showed that a strong west Pacific subtropical high (WPSH) was unfavourable for the formation of O_3 in South China (Zhao and Wang, 2017), however the physical mechanisms to impact O_3 in North China was still not sufficiently explained. Thus, in addition to human activities and secondary aerosol processes, the impacts of atmospheric circulations and meteorological conditions must be systematically studied to improve understanding of the O_3 pollution in North China.

Since 2015, O_3 measurements in eastern China were steadily and widely implemented, but the O_3-weather studies mainly focused on meteorological elements (e.g. temperature, precipitation etc.) and several synoptic processes (Xu et al., 2017; Xiao et al., 2018; Pu et al., 2017). The dominant patterns of daily ozone in summer in east of China are still unclear. In this study, we built upon the previous literatures analysing ozone and meteorological influences thanks to the availability of more ozone observations by the Chinese government since 2015, providing us more information to analyse than available in these earlier studies, e.g., Zhao and Wang (2017). The findings of this study basically help to understand the varying features of daily surface ozone pollution in eastern China and their relationships with large-scale atmospheric circulations.

2. Data sets and methods

Nationwide hourly O_3 concentration data since May 2014 are publicly available on http://beijingair.sinaapp.com/. Since the severe air pollution events in 2013, the air pollution issues gained more attentions from the Chinese government and society, which aided to start the extensive constructions of operational monitoring stations of atmospheric components and resulted in continuous increasing number of sites (Figure S1). The number of sites in eastern China (110ºE–125ºE, 22ºN–42ºN) was 677, 937, 937, 995 and 1007 from 2014 to 2018. It is obvious that the data in 2014 were deficient, while the observations were broadly distributed in eastern China and continuously achieved since 2015. Thus, the summer O_3 data from 2015 to 2018 were processed (e.g., unifying the sites and eliminating the missing value) and 868 sites in eastern China were employed here to reveal some new features of surface ozone pollutions and associated anomalous atmospheric circulations. Generally, severe air pollutions occurred more frequently in cites than in rural areas, therefore, the monitoring sites of atmospheric components mostly gathered around the urban areas, indicating the results of this study were more suitable for the urban O_3 pollution. The maximum daily average 8 h concentration of ozone (MDA8) is the maximum of the running 8 h mean O_3 concentration during an entire 24 hour day. According to the Technical Regulation on Ambient Air Quality Index of China (the Ministry of Environmental Protection of China, 2012), MDA8 is generally used to represent the daily O_3 conditions. The MDA8 $\in$ [0, 100], (100, 160], (160, 215], (215, 265], (265, 800] μg/m³ corresponds to “Excellent”, “Good”, “Lightly polluted”, “Moderately polluted”, “Heavily polluted” levels of air quality in China.

The 2.5°×2.5° ERA-Interim data used here include the geopotential height (Z) at 850 and 500 hPa, zonal and meridional wind, relative humidity, vertical velocity, air temperature from surface to 100 hPa, surface air temperature (SAT) and wind, downward solar radiation at the surface, low and medium cloud cover and precipitation (Dee et al., 2011). Because the maximum photochemical activity often occurred at afternoon (Wang et al., 2010), the daytime data were calculated by the 6-hourly reanalysis (including Z, wind, relative humidity, vertical velocity, air temperature and cloud cover) and 3-hourly data (precipitation and downward solar radiation) to composite the daytime atmospheric circulations and daytime meteorological conditions. The daytime of the ERA-Interim variables was unified as 05–17 (Beijing Time; 21–09 UTC).

The empirical orthogonal function (EOF) analysis is a widely used statistical method in meteorology to reconstruct the original variables into several irrelevant patterns (Wilks, 2011). The EOF analysis, applied to the daily anomalies (MDA8 anomalies at 868 stations in this study）, extracted the relative change features of the original data on the daily time-scale. The orthogonal modes included spatial and temporal coefficients, and contained information of some proportion (variance contributions) from the original fields. Significance test must be execute to confirm whether the decomposed patterns had physical meanings. In this study, we used the test method form North et al. (1982). That is, if the eigenvalue (λ) satisfied the condition as $\lambda_i - \lambda_{i+1} \geq \lambda_i (2/n)^{1/2}$, the eigenvalue λ_i was significantly separated. We performed this significance test on the selected patterns from EOF decompositions, and confirmed that these dominant patterns in this study were all significant. The aforementioned EOF analysis programs were finished by the NCAR Command Language.

3. Variations and dominant patterns

During 2015–2018, summer surface ozone pollution was severe in China, especially in the economically developed regions. Spatially, the JJA mean MDA8 increased from south to north in eastern China (Figure 1a). To the south of 28°N (i.e., South China), the mean MDA8 was mostly lower than 100 μg/m³ and lower than the O_3 pollution in North China and in the Huanghuai area (NCH, Figure 1a). It is notable that, although the values of MDA8 in the PRD were not as large as those in NCH, they were relatively higher than those in the surrounding areas. The mean MDA8 was above 110 μg/m³ to the north of 32°N (i.e., the NCH area), and thereinto, the large values of MDA8 centred on the Beijing-Tianjin-Hebei region and in western Shandong province exceeded 150 μg/m³. In the transitional zone, i.e., between 28°N and 32°N, the MDA8 varied from 100 μg/m³ to 120 μg/m³. Surface O_3 pollution was closely linked to the anthropogenic emissions that dispersed and concentrated in the large cities (Fu et al., 2012), which was similar to the haze pollution (Yin et al., 2015). In the megacity cluster, the photochemical regime for ozone formation is combination of NO_x-limited and VOC-limited regimes (Jin and Holloway 2015). In the YRD and PRD, high levels of MDA8 were scattered around the large cities. Due to high emissions of NO_x both in large and small cities in the NCH region, the high-level O_3 values were contiguous, indicating extensively surface O_3 pollution (Figure 1). Furthermore, the maximum values of MDA8 for four summers were extracted to evaluate the severest levels of O_3 pollution (Figure 1b). To the north of 30°N, the maximum MDA8 at most sites was above 265μg/m³ (i.e., the threshold of heavily O_3 pollution in China), indicating that heavily O_3 pollution had occurred. The observed summer MDA8 anomalies in eastern China also presented evident interannual differences (Figure 2). The number of sites with maximum MDA8 > 265 μg/m³ in NCH (YRD) was 94 (35), 55 (22), 180 (58), 160 (46) from 2015 to 2018 (Figure 2). The summer mean MDA8 in the PRD was not as high as that in NC and the YRD (Figure 1a), but maximum O_3 concentration exceeded 265 μg/m³ could also be observed in certain large cities of PRD in each year (Figure 2).

Ten cities, with O_3 pollutions, were chosen to investigate the temporal variations, including Beijing (capital of China), Tangshan, Tianjin near the capital city, Shijiazhuang, Weifang and Taiyuan in the south of NCH, Nanjing and Shanghai in YRD, Guangdong and Zhongshan in PRD (Figure S2). These cities had large populations and were with high levels of O_3 pollutions. In Beijing, Tianjin and Tangshan, the MDA8 values were nearly above 100 μg/m³ and frequently exceeded 215 μg/m³ (Figure 3a). The percentage of non-O_3-polluted days (<100 μg/m³) and moderate O_3-polluted days (>215 μg/m³) were 14.9% and 15.5% for the mean MDA8 of these three cities. The former percentage indicated that more than 85% O_3 concentrations exceeded the health threshold (i.e., the upper limit “Excellent” level), and the later meant, in more than 15% of summer days, O_3 concentrations moderately damaged human health in the Beijing-Tianjin-Hebei region. The maximum MDA8 in the north of Hebei province (e.g. Tangshan in Figure 3a) and in eastern Shandong province (e.g. Weifang in Figure 3b) even exceeded 320 μg/m³, which badly injured the health of local citizens. In Shijiazhuang, Weifang and Taiyuan, the MDA8 levels were lower than those in Beijing and Tianjin during 2015–2016, but dramatically increased to levels comparable to those of Beijing and Tianjin in 2017 and 2018 (Figure 3a, b). In Nanjing and Shanghai, the MDA8 did not show a clear increasing trend (Figure 3c). Similar to the distribution of the mean MDA8, the maximum MDA8 to the south of 30°N was lower by comparison. Although approximately 60% of summer days were non-O_3-polluted in the cities of Guangzhou and Zhongshan (Figure 3d), heavily polluted O_3 pollution also occurred in the PRD (Figure 1b).

Considering the characteristics of the observed MDA8 mentioned above, EOF approach was used to explore the dominant patterns of summer ozone pollution in eastern China (Figure 4). The percentages of variance contribution for the first three patterns were 21.5%, 15.5% and 8%. The significance test of the EOF eigenvalues confirmed that the first three patterns were significantly separated. Approximately 37% of the variability in the original data was contained in the first two patterns, therefore, they were defined as the dominant patterns of surface ozone pollution on the daily time-scale. In the first EOF pattern (PAT1), the observed MDA8 at different sites changed similarly and the centre of variation was located in the NCH area (Figure 4a). The time series of EOF1 showed that the ozone pollution during 2017–2018 was more serious than that in 2015 and 2016 (Figure 4b). Differently, the second EOF pattern (PAT2), showed notable south-north difference, with centres in the NC and YRD regions (Figure 4c). The time coefficient of PAT2 did not show an obvious increasing trend (Figure 4d). The positive (P) and negative (N) phases of PAT1 (PAT1P, PAT1N) and PAT2 (PAT2P, PAT2N) are defined by the events that are greater than one standard deviation and less than –1 ×one standard deviation, respectively (Figure 4b, 4d).

Figure 4 illustrates the EOF results for the dominant patterns of surface ozone, while Figure 5 show the MDA8 composites break down into the positive and negative phases. The ozone concentrations for the PAT1P classification (Figure 5a) were generally greater than those for PAT1N (Figure 5b). Most of the MDA8 values in the NCH region were >160 μg/m³ and <120 μg/m³ for PAT1P and PAT1N, respectively (Figure 5a, b). For the second pattern, the PAT2P appeared as a diminishing pattern from the north to the south (Figure 5c), however, there was high concentrations of ozone pollution in the YRD and PRD under PAT2N conditions (Figure 5d). Therefore, the centres of O_3 variation were NCH for the PAT1, and NC and the YRD for the PAT2.

4. Associated atmospheric circulations

In eastern China, despite the economic productions and human actives steadily increased in the four years of study and we assume the emissions of ozone precursors to be relatively stable on the daily time-scale. Differently, the daily variations in MDA8 were evidently saw in Figure 3. Therefore, the impacts of daily meteorological conditions significantly contributed to the domain patterns of daily O_3 concentrations and their variations. Anomalous daytime atmospheric circulations associated with PAT1 (PAT1P composite minus PAT1N composite) and PAT2 (PAT2P composite minus PAT2N composite) are shown Figure 6–7. For the first pattern, the largest O_3 differences between the PAT1P and PAT1N was within the NCH region (Figure 5a, b). The correlation coefficient between the time series of PAT1 and the NCH-averaged MDA8 was 0.97 (Table 1). Thus, the effects of the anomalous atmospheric circulations mainly acted on the photochemical reactions near the surface in NCH and the removal of pollutants. In Figure 6a, there were negative Z850 anomalies over the Ural Mountains. Over the broad region from eastern Eurasia to the north Pacific, the anomalous atmospheric circulations were located zonally, i.e., positive Z850 on the tropical zone, cyclonic anomalies at the mid to high latitudes and positive anomalies on the polar region (Figure 6a). The East Asia deep trough was enhanced and extended to northeast China and Japan. The intensity of the East Asia deep trough (i.e., the negative area-averaged Z850) positively correlated with the time series of PAT1 (EAT, Table 1) with a correlation coefficient of 0.28 (above the 99% confidence level). In accordance with the deep positive height anomalies to the north of Lake Baikal (centring at 107 ^{o}E, 53.5 ^{o}N), which also extended southward to the edge of the Tibetan Plateau (Figure 6a), cold air was transported to the lower latitudes. However, local anti-cyclonic circulation over NCH prevented the cold air to arrive at the NCH region (Figure 6b).

Influenced by the enhanced East Asia deep trough, the main body of WPSH shifted southward (compared to its climate status in summer). The location of WPSH ($Z500_{(125^{0}E,\ 20^{0}N)} - Z500_{(125^{0}E,\ 30^{0}N)}$) also showed a positive correlation with the time series of PAT1 (R=0.39, Table 1). However, the western ridge point of WPSH was northward and westward than normal (being indicated by$Z500_{(110^{0}E,\ 30^{0}N)}$), and occupied the NCH area, which was significant with the time series of PAT1 (R=0.24, above the 99% confidence level). Although the local anomalous anticyclone over the east of China seemingly delivered water vapor to North China (Figure 6b), the channel of moisture was already cut off in the ocean at low latitudes by the positive and zonal anomalies in the tropical regions (Figure 6a) and resulted in a dry environment in NCH from surface to 400 hPa (Figure 6c). Furthermore, the associated descending motions (Figure 6c) not only corresponded to the warmer surface air temperature (Figure 6a), but also suppressed the development of convective activity (indicating by less low and medium cloud, Figure 6d). The correlation coefficients between the time series of PAT1 and NCH-averaged precipitation, SAT, and downward solar radiation at surface were –0.44, 0.14 and 0.45, respectively, all of which exceeded the 99% significance test (Table 1). The large-scale atmospheric circulations led to days with high temperatures near the surface (Figure 6a), less precipitation (Figure 6b), a dry environment (Figure 6c) and intense solar radiation (Figure 6d), which substantially enhanced the generation of ozone in NCH but weakened the removal of the pollutants.

For PAT2, largest O_3 differences (PAT2P composite minus PAT2N composite) were observed in the NC and YRD regions (Figure 4c, Figure 5c, d). The correlation coefficient between the time series of PAT2 and the MDA8 difference between NC and the YRD was 0.77 (Table 1). The impacts of atmospheric circulations on the photochemical reactions and removal effects in the above two areas are analysed in Figure 7. It is notable that the signals of atmospheric circulations were clearer at the lower troposphere (i.e., 850 hPa) for PAT1 (Figure 6a), however, the signals for PAT2 could be recognized both at the low- and mid- troposphere (Figure 7a). Due to the broad positive Z500 anomalies at the high latitudes of Eurasia, the subjacent surface air temperatures significantly increased, indicating weak cold air advection from the north (Figure 7a). Moreover, there were positive Z500 anomalies from the Chukchi Peninsula (about cantering at 180 °E, 66.5 °N) to Northeast China. In summer, anomalous anticyclonic circulations at the mid and high latitudes generally led to significantly positive SAT anomalies (Figure 7a). The East Asia deep trough was stronger (R=0.3), but was limited to the Sea of Japan.

Extruded by the East Asia deep trough and cyclonic anomalies from the Siberian plains to the YRD, the WPSH moved southward and exhibited southwest-northeast orientation (Figure 7a). The location of WPSH ($Z500_{(110^0E,\ 20^0N)} - Z500_{(110^0E,\ 30^0N)}$) was positively correlated with the time series of PAT2 (R=0.32, Table 1). The southwest-northeast distribution of WPSH aided water vapor transportation to the YRD region (Figure 7b–c). Combined with significant upward air flow (Figure 7c), more clouds formed at the medium and low levels (Figure 7d) and precipitation was enhanced in the YRD region (Figure 7b). A moist-cool environment, weak solar radiation and wet deposition reduced the ozone concentration in the YRD region. On the other hand, sinking motion (Figure 7c) and less cold air advection from the north (Figure 7a) both resulted in a temperature increase in NC (Figure 7a). There was divergence of water vapor and less cloud cover over NC, resulting in dry, hot and sunny weather (Figure 7b, d). Under such meteorological conditions, the generation of surface O_3 was accelerated but the removal processes were slowed down, and thus, higher MDA8 was observed in NC. The differences in precipitation, SAT, and downward solar radiation at the surface between the NC and YRD regions were calculated and their correlation coefficients with the time series of PAT2 were –0.46, 0.18 and 0.62, respectively (Table 1). The significant correlations indicated that the differences in meteorological conditions between NC and YRD regions, associated with the aforementioned anomalous atmospheric circulations, largely contributed to O_3 PAT2.

5. Conclusions and discussions

At present, the fine particulate matter decreased in the summers in eastern China, and ground-level ozone pollution became the major air challenge in the summers in the east of China (Li et al., 2018). The highest O_3 concentrations were observed in North China and in the Huanghuai region, which are located north of 32°N. The O_3-contaminated air occurred for 85% of summer days in Beijing and Tianjin. In the south, the surface O_3 pollution was also severe both in the Yangtze and

Pearl River delta regions. Meteorological conditions had significant impacts on the evident daily fluctuation of MDA8. To reveal their detailed relationships, the dominant patterns of summer ozone pollution and associated atmospheric circulations were analysed in this study.

The MDA8 of the first prominent pattern changed synergistically in the east of China, especially in North China and Huanghuai region. An enhanced East Asia deep trough and west Pacific subtropical high were zonally distributed and prevented the northward transportation of moisture. The northward-shifted western ridge point of the west Pacific subtropical high accelerated the photochemical reactions via hot-dry air and intense solar radiation, but weaken the removal of pollutants. The second pattern of ozone pollution showed remarkable south-north differences. Broad positive geopotential height anomalies at the high latitudes significantly decreased cold air advection from the north and thus increased the surface air temperature. These positive anomalies also extended to North China and resulted in locally warmer air near the surface. On the other hand, the southwest-northeast oriented west Pacific subtropical high transported sufficient water vapor to the Yangtze River Delta. Consequently, a local moist-cool environment, without intense sunlight, reduced the formation of surface ozone.

In addition to evident interannual differences of MDA8 anomalies (Figure 2), the dominant spatial patterns of MDA8 anomalies in each year were also different (Figure 8). Although the relative variance contributions of the spatial coefficients varied, the first two EOF patterns of MDA8 were always PAT1 and PAT2 in different years, indicating that the extracted dominant patterns were reliable and steady. Sorting by the variance contribution, the dominant patterns were PAT2 and PAT1 in 2015 and 2016 (Figure 8a–d), however, they are PAT1 and PAT2 in the two subsequent years (Figure 8e–h). The first EOF pattern in 2014 revealed by Zhao and Wang (2017) was similar with PAT2, however the most dominant pattern changed to PAT1 in the latest two years (2017 and 2018). In 2016 and 2018, the variance contribution of the first pattern was almost twice that of the second pattern. The dominant pattern of 2016 was PAT2 (explaining approximately 24% of the variance, Figure 8c), while that in 2018 changed as PAT1, with nearly 34% variance contributions (Figure 8g). In 2016, the MDA8 values in NC and the YRD were nearly out of phase (Figure 9a), and the correlation coefficient between them was –0.28 (above the 99% confidence level). Differently, this correlation coefficient was 0.43 in 2018 (Figure 9b), indicating similar change features between the MDA8 levels of NC and the YRD. The dominant patterns of ozone concentrations were decomposed with the observed data from 2015 to 2018. With the increase in O_3 observations, increasingly reliable dominant patterns and the reasons for the variation in dominant patterns might be revealed in the future.

In this study, we mainly emphasized the contribution of the meteorological impacts and assumed the emissions of ozone precursors were relatively stable on the daily time-scale. Observational and modelling studies suggested that photochemical production of ozone in the NC, YRD and PRD was the transitional regime (i.e., both reductions of NO_x and VOC would reduce O_3), which would influence the concentrations of surface ozone (Jin and Holloway 2015). There is no doubt that the human activities were the fundamental driver of air pollution even on the daily time-scale, thus the joint effects of the daily meteorological conditions and anthropogenic emissions (including the photochemical regimes) needed to be discussed in future work. Lu et al. (2019) found that the observed 2017 surface ozone increases relative to 2016 in China are largely due to hotter and drier weather conditions, while changes in domestic anthropogenic emissions alone would have led to ozone decreases in 2017 basing on their GEOS-Chem experiments. The simultaneous large-scale atmospheric circulations on an interannual scale and their possible preceding climate drivers, e.g., sea ice, and sea surface temperature, were still unclear so far. The research related to climate variability has always needed long-term data. To get around the problem of the data time span, Yin et al. (2019) developed an ozone weather index using data from 1979 to 2017 and demonstrated the contributions of Arctic sea ice in May to O_3 pollution in North China. According to the results, attentions to surface pollution should be strengthened and the weather-climate component should be taken into account when making decisions for control measures.

Data availability.

Hourly O_3 concentration data is supported by the website: http://beijingair.sinaapp.com (Ministry of Environmental Protection of China, 2018). Atmospheric circulation datasets are downloaded from http://www.ecmwf.int/en/research/climate-reanalysis/era-interim (ERA-Interim, 2018).

Author contribution.

ZY and HW designed the research. BC and ZY performed most of the Figures and analysis. ZY prepared the paper with contributions from all co-authors.

Competing interests.

The authors declare that they have no conflict of interest.

Acknowledgements.

This research was supported by the National Natural Science Foundation of China (41421004, 91744311 and 41705058) and the funding of the Jiangsu Innovation & Entrepreneurship team.

References

Day, D. B., Xiang, J. B., Mo, J. H., Li, F., Chung, M., Gong, J. C., Weschler, C. J., Ohman-Strickland, P. A., Sundell, J., Weng, W. G., Zhang, Y. P., and Zhang J.: Association of Ozone Exposure with Cardiorespiratory Pathophysiologic Mechanisms in Healthy Adults. JAMA Internal Medicine, 177(9), 1344-1353, doi:10.1001/jamainternmed.2017.2842, 2017.

Dee, D. P., Uppala, S. M., Simmons, A. J., Berrisford, P., Poli, P., Kobayashi, S., Andrae, U., Balmaseda, M. A., Balsamo, G., Bauer, P., Bechtold, P., and Beljaars, A. C. M.: The ERAInterim reanalysis: configuration and performance of the data assimilation system, Quarterly Journal of the Royal Meteorological Society, 137, 553–597, doi:10.1002/qj.828, 2011.

Ding, A. J., Fu, C. B., Yang, X. Q., Sun, J. N., Zheng, L. F., Xie, Y. N., Herrmann, E., Nie, W., Petäjä, T., Kerminen, V. M., and Kulmala, M.: Ozone and fine particle in the western Yangtze River Delta: an overview of 1 yr data at the SORPES station, Atmospheric Chemistry and Physics, 13(11), 5813-5830, doi:10.5194/acp-13-5813-2013, 2013.

Ding, A. J., Wang, T., Zhao, M., Wang, T. J., Li, Z. K.: Simulation of sea-land breezes and a discussion of their implications on the transport of air pollution during a multi-day ozone episode in the Pearl River Delta of China, Atmospheric Environment, 38(39):6737-6750, doi:10.5194/acpd-13-2835-2013, 2004.

Doherty, R. M., Wild, O., Shindell, D. T., Zeng, G., MacKenzie, I. A., Collins, W. J., Fiore, A. M., Stevenson, D. S., Dentener, F. J., Schults, M. G., Hess, P., Derwent, R. G., Keating, T. J.: Impacts of climate change on surface ozone and intercontinental ozone pollution: A multi-model study, Journal of Geophysical Research Atmospheres, 118(9), 3744–3763, doi:10.1002/jgrd.50266, 2013.

Fu, J.S., Dong, X., Gao, Y.,Wong, D.C., Lam, Y.F. Sensitivity and linearity analysis of ozone in East Asia: the effects of domestic emission and intercontinental transport. J. AirWaste Manage. Assoc. 62, 1102–1114, 2012

Gao, W., Tie, X. X., Xu, J. M., Huang, R. J., Mao, X. Q., Zhou, G. Q., Chang, L. Y.: Long-term trend of O_3 in a mega City (Shanghai), China: Characteristics, causes, and interactions with precursors, Science of the Total Environment, 603–604,425–433, doi:10.1016/j.scitotenv.2017.06.099, 2017.

Jin, X. M., Holloway T., Spatial and temporal variability of ozone sensitivity over China observed from the Ozone Monitoring Instrument, Journal of Geophysical Research: Atmospheres, 120, 7229–7246, doi:10.1002/2015JD023250, 2015.

Li, J. F., Lu, K. D., Lv, W., Li, J., Zhong, L. J., Ou, Y. B., Chen, D. H., Huang, X., Zhang, Y. H.: Fast increasing of surface ozone concentrations in Pearl River Delta characterized by a regional air quality monitoring network during 2006–2011, Journal of Environmental Sciences, 26, 23–36, doi:10.1016/S1001-0742(13)60377-0, 2014.

Li, K., Jacob, D. J., Liao, H., Shen, L., Zhang, Q., Bates, K. H.: Anthropogenic drivers of 2013–2017 trends in summer surface ozone in China, Proceedings of the National Academy of Sciences of the United States of America, 116(2), 422-427, doi:10.1073/pnas.1812168116, 2018

Lin, M. Y., Fiore, A. M., Horowitz, L. W., Langford, A. O., Oltmans, S. J., Tarasick, D., and Rieder, H. E.: Climate variability modulates western US ozone air quality in spring via deep stratospheric intrusions, Nature Communications, 6(1), 7105-7105, doi:10.1038/ncomms8105, 2015.

Lu, X., Hong, J. Y., Zhang, L., Cooper, O. R., Schultz, M. G., Xu, X. B., Wang, T., Gao, M., Zhao, Y. H., Zhang, Y. H. Severe surface ozone pollution in China: A global perspective, Environmental Science & Technology Letters, 5, 487–494, doi:10.1021/acs.estlett.8b00366, 2018.

Lu, X., Zhang, L., Chen, Y., Zhou, M., Zheng, B., Li, K., Liu, Y., Lin, J., Fu, T.-M., and Zhang, Q.: Exploring 2016–2017 surface ozone pollution over China: source contributions and meteorological influences, Atmos. Chem. Phys., 19, 8339–8361, https://doi.org/10.5194/acp-19-8339-2019, 2019.

Ma, Z. Q., Xu, J., Quan, W. J., Zhang, Z. Y., Lin, W. L., and Xu, X. B.: Significant increase of surface ozone at a rural site, north of eastern China, Atmospheric Chemistry and Physics, 16(6), 3969–3977, doi:10.5194/acp-16-3969-2016, 2016.

North, G. R. , Bell, T. L. , Cahalan, R. F. , Moeng, F. J. Sampling errors in the estimation of empirical orthogonal functions. Monthly Weather Review, 110(7), 699-706, 1982

Pu, X., Wang, T. J., Huang, X., Melas, D., Zanis, P., Papanastasiou, D. K., Poupkou, A.: Enhanced surface ozone during the heat wave of 2013 in yangtze river delta region, china, Science of the Total Environment, 603, 807–816, https://doi.org/10.1016/j.scitotenv.2017.03.056, 2017.

Shi, C. Z., Wang, S. S., Liu, R., Zhou, R., Li, D. H., Wang, W. X., Li, Z. Q., Cheng, T. T., Zhou, B.: A study of aerosol optical properties during ozone pollution episodes in 2013 over Shanghai, China. Atmospheric Research, 153, 235–249, doi:10.1016/j.atmosres.2014.09.002, 2015.

Sun, L., Xue, L. K., Wang, T., Gao, J., Ding, A. J., Cooper, O. R., Lin, M. Y., Xu, P. J., Wang, Z., Wang, X. F., Wen, L., Zhu, Y. H., Chen, T. S., Yang, L. X., Wang, Y., Chen, J. M., and Wang, W. X.: Significant increase of summertime ozone at Mount Tai in Central Eastern China, Atmospheric Chemistry and Physics, 16, 10637-10650, doi:10.5194/acp-16-10637-2016, 2016.

The Ministry of Environmental Protection of China: Technical Regulation on Ambient Air Quality Index, China Environmental Science Press, China, 2012

Tong, L., Zhang, H. L., Yu, J., He, M. M., Xu N. B., Zhang, J. J., Qian F. Z., Feng J. Y., and Xiao, H.: Characteristics of surface ozone and nitrogen oxides at urban, suburban and rural sites in Ningbo, China, Atmospheric Research, 187: 57–68, https://doi.org/10.1016/j.atmosres.2016.12.006, 2017.

Wang, T., Ding, A., Gao, J., Wu, W. S.: Strong ozone production in urban plumes from Beijing, China, Geophysical Research Letters, 33(21), 320–337, doi:10.1029/2006GL027689, 2006.

Wang, T., Nie, W., Gao, J., Xue, L. K.: Air quality during the 2008 Beijing Olympics: secondary pollutants and regional impact. Atmospheric Chemistry and Physics, 10(16), 7603-7615, doi:10.5194/acp-10-7603-2010, 2010.

Wang, T., Xue, L. K., Brimblecombe, P., Lam, Y. F., Li, L., Zhang, L.: Ozone pollution in China: A review of concentrations, meteorological influences, chemical precursors, and effects, Science of The Total Environment, 575, 1582-1596, doi:10.1016/j.scitotenv.2016.10.081, 2017.

Wang, Y. X., Shen, L. L., Wu, S. L., Mlckley, L., He, J. W., and Hao, J. M.: Sensitivity of surface ozone over China to 2000–2050 global changes of climate and emissions, Atmospheric Environment, 75, 372–382, doi:10.1016/j.atmosenv.2013.04.045, 2013.

Wilks, D.S., 2011. Statistical Methods in the Atmospheric Sciences. Academic press.

Xiao, Z. , Wang, Z. , Pan, W. , Wang, Y. , Yang, S. Sensitivity of extreme temperature events to urbanization in the pearl river delta region. Asia-Pacific Journal of the Atmospheric Sciences., 2018

Xu, Z. , Huang, X. , Nie, W. , Chi, X. , Xu, Z. , Zheng, L. , et al. Influence of synoptic condition and holiday effects on vocs and ozone production in the Yangtze river delta region, china. Atmospheric Environment, S1352231017305496, 2017

Yang, Y., Liao, H., Li, J. P.: Impacts of the East Asian summer monsoon on interannual variations of summertime surface-layer ozone concentrations over China. Atmospheric Chemistry and Physics, 14:6867–6879, doi:10.5194/acp-14-6867-2014, 2014.

Yin, Z. C., Wang, H. J., and Guo, W. L.: Climatic change features of fog and haze in winter over North China and Huang-Huai Area, Sci. China. Earth. Sci., 58(8): 1370–1376, 2015.

Yin, Z. C., Wang, H. J., Li, Y. Y., Ma, X. H., Zhang, X. Y.: Links of Climate Variability among Arctic sea ice, Eurasia teleconnection pattern and summer surface ozone pollution in North China, Atmospheric Chemistry and Physics, 19, 3857–3871, https://doi.org/10.5194/acp-19-3857-2019, 2019.

Yue X, Unger, N., Harper, K., Xia, X. G., Liao, H., Zhu, T., Xiao J. F., Feng, Z. Z., and Li, J.: Ozone and haze pollution weakens net primary productivity in China, Atmospheric Chemistry and Physics, 17:6073–6089, doi:10.5194/acp-2016-1025, 2017.

Zhao, Z. J., Wang, Y. X.: Influence of the west pacific subtropical high on surface ozone daily variability in summertime over eastern china, Atmospheric Environment, 170, 197–204, https://doi.org/10.1016/j.atmosenv.2017.09.024, 2017.

Figures captions

Table 1. Correlation coefficients between the time series of PAT1 (PAT2) and the key indices of atmospheric circulations and meteorological conditions. “**” and “*” indicate that the correlation coefficients were above the 99% and 95% confidence level, respectively.

Figure 1. Distribution of the (a) mean values and (b) maximum values of MDA8 (Unit: $\mu g/m^3$) at the observation sites in summer from 2015 to 2018. The black boxes in panels a and b indicated the locations of North China and Huanghuai region (NCH), North China (NC), Yangtze River Delta (YRD) and Pearl River Delta (PRD).

Figure 2. Anomalies of the summer mean MDA8 (Unit: $\mu g/m^3$) in 2015 (a), 2016 (b), 2017 (c) and 2018 (d), relative to the mean during 2015–2018. The black pluses indicate that the maximum MDA8 was larger than 265 $\mu g/m^3$. The black boxes in panel b indicated the locations of NC, YRD and PRD, while that in panel d was the NCH area.

Figure 3. Variations in MDA8 (Unit: $\mu g/m^3$) of polluted cities from 2015 to 2018, including (a) Beijing (capital of China), Tianjin and Tangshan near the capital city; (b) Taiyuan, Weifang and Shijiazhuang in the south of NCH; (c) Shanghai and Nanjing in YRD; and (d) Zhongshan and Guangzhou in PRD. The cities in panels (a)-(d) were located from north to south and were illustrated in Figure S2. The horizontal dash lines indicated the value of 100 $\mu g/m^3$ and 215 $\mu g/m^3$.

Figure 4. The first EOF pattern (PAT1: a, b) and second EOF pattern (PAT2: c, d) of MDA8 in summer from 2015 to 2018, including the spatial pattern (a, c) and the time coefficient (b, d). The black boxes in panels a and c are the selected North China and Huanghuai region (NCH), North China (NC), Yangtze River Delta (YRD) and Pearl River Delta (PRD). The EOF analysis were applied to the daily MDA8 anomalies at 868 stations to extract the relatively change features of the original data on the daily time-scale. The percentages on panel (b) and (d) were the variance contributions of the first and second EOF mode. The horizontal dash lines indicated one standard deviation, and the vertical ones separated the years.

Figure 5. Composites of the MDA8 (Unit: $\mu g/m^3$) for PAT1 (a, b) and PAT2 (c, d) in summer from 2015 to 2018. Panels (a) and (c) were composited when the time coefficient of EOF1 and EOF2 was greater than one standard deviation, while panels (b) and (d) were composited when the time coefficient was less than $-1\times$one standard deviation. The black box in panel a-b indicated the location of NCH, while those in panel c-d were the NH, YRD and PRD area.

Figure 6. Differences of the daytime atmospheric circulations (i.e., PAT1P minus PAT1N). (a) Geopotential height at 850 hPa (Unit: 10gpm, contours) and surface air temperature (Unit: K, shading), (b) water vapor flux (Unit:$gs^{-1}cm^{-1}hpa^{-1}$) at 850 hPa (arrows) and precipitation (Unit: mm, shading), (c) 100°E–120°E mean wind (Unit: m/s, arrows) and relative humidity (Unit: %, shading), (d) downward solar radiation at the surface (Unit:10^7 J/m^2, shading) and the sum of low and medium cloud cover (Unit: 1, contours). The white dots indicate that the shading was above the 95% confidence level. The green boxes in panels (a), (b) and (d) show the NCH region, and the black box in panel (a) indicates the location of the East Asia trough. The purple triangles in panel (a) indicated the data used to calculate the $WPSH_1$, while the red triangle represented the west ridge point of WPSH.

Figure 7. Differences of the daytime atmospheric circulations (i.e., PAT2P minus PAT2N). (a) Geopotential height at 500 hPa (Unit: 10gpm, contours) and surface air temperature (Unit: K, shading), (b) water vapor flux (Unit:$gs^{-1}cm^{-1}hpa^{-1}$) at 850 hPa (arrows) and precipitation (Unit: mm, shading), (c) 100°E–120°E mean wind (Unit: m/s, arrows) and relative humidity (Unit: %, shading), (d) downward solar radiation at the surface (Unit: $10^7 J/m^2$, shading) and the sum of low and medium cloud cover (Unit: 1, contours). The white dots indicate that the shading was above the 95% confidence level. The green boxes in panel (a), (b) and (d) are the NC and YRD regions, and the black box in panel (a) indicates the location of the East Asia trough. The purple triangles in panel (a) indicated the data used to calculate the $WPSH_2$.

Figure 8. The first (a, c, e, g) and second (b, d, f, h) EOF spatial patterns of MDA8 in summer in 2015 (a, b), 2016 (c, d), 2017, (e, f) and 2018(g, h). The percentage number in panels (a, c, e, g) and (b, d, f, h) are the variance contributions of the first and second EOF mode. The black boxes indicated the location of NCH, NH, YRD and PRD, respectively.

Figure 9. Variations in the MDA8 (Unit: $\mu g/m^3$) of NC (black) and the YRD (blue) in 2016 (a) and 2018 (b). The MDA8 was calculated as an average for all available sites in the NC and the YRD regions.

Table 1. Correlation coefficients between the time series of PAT1 (PAT2) and the key indices of atmospheric circulations and meteorological conditions. "**" and "*" indicate that the correlation coefficients were above the 99% and 95% confidence level, respectively.

PAT1	**$MDA8_1$**	**EAT_1**	**$WPSH_1$**	**Pre_1**	**SAT_1**	**SSR_1**
	0.97^{**}	0.28^{**}	0.39^{**}	-0.44^{**}	0.14^{**}	0.64^{**}
PAT2	**$MDA8_2$**	**EAT_2**	**$WPSH_2$**	**Pre_2**	**SAT_2**	**SSR_2**
	0.77^{**}	0.30^{**}	0.32^{**}	-0.49^{**}	0.18^{**}	0.65^{**}

$MDA8_1$ is the NCH-area averaged MDA8, while the $MDA8_2$ is the MDA8 difference between NC and YRD. EAT_1 and EAT_2 indicate the intensity of the East Asia deep trough and were calculated as the mean –Z850 shown in the black boxes in Figure 5 and Figure 6, respectively. $WPSH_1$ ($Z500_{(125^oE,\ 20^oN)} - Z500_{(125^oE,\ 30^oN)}$) and $WPSH_2$ ($Z500_{(110^oE,\ 20^oN)} - Z500_{(110^oE,\ 30^oN)}$) represents the location of WPSH. Pre_1, SAT_1 and SSR_1 were calculated as the NCH-area averaged precipitation, SAT and downward solar radiation at the surface, respectively. Pre_2, SAT_2 and SSR_2 are the differences in the NC- and YRD-area averaged precipitation, SAT and downward solar radiation at the surface, respectively.

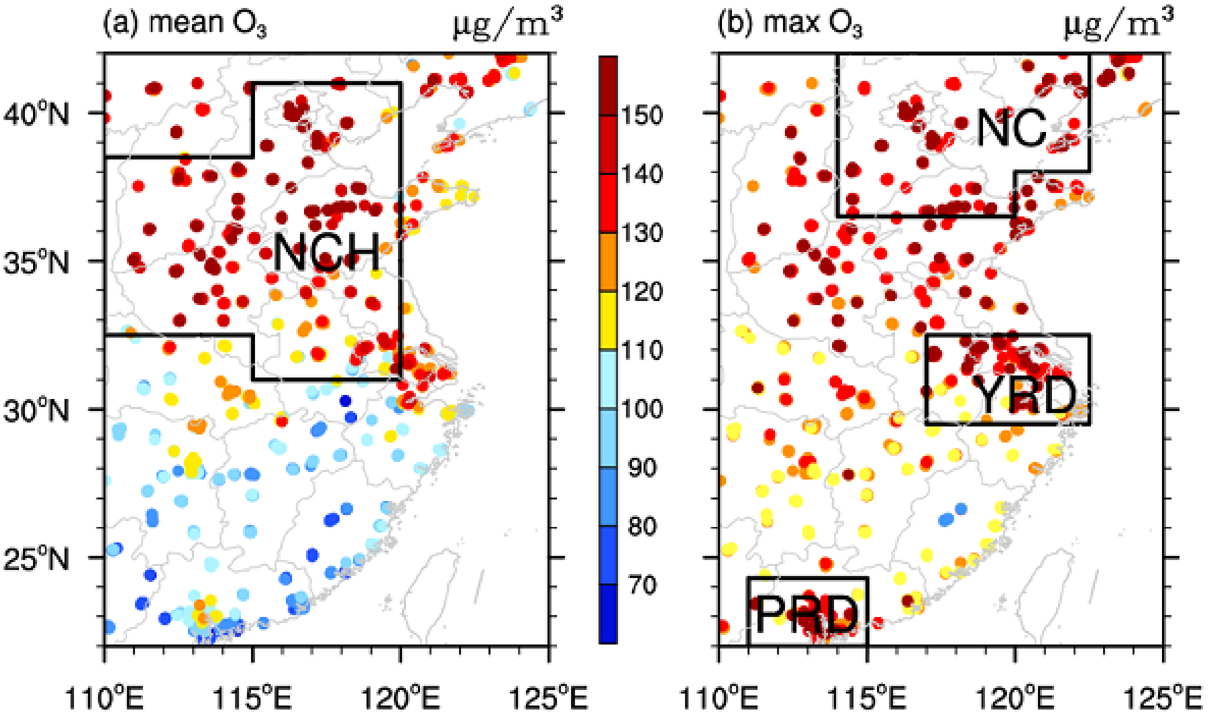

Figure 1. Distribution of the (a) mean values and (b) maximum values of MDA8 (Unit: µg/m³) at the observation sites in summer from 2015 to 2018. The black boxes in panels a and b indicated the locations of North China and Huanghuai region (NCH), North China (NC), Yangtze River Delta (YRD) and Pearl River Delta (PRD).

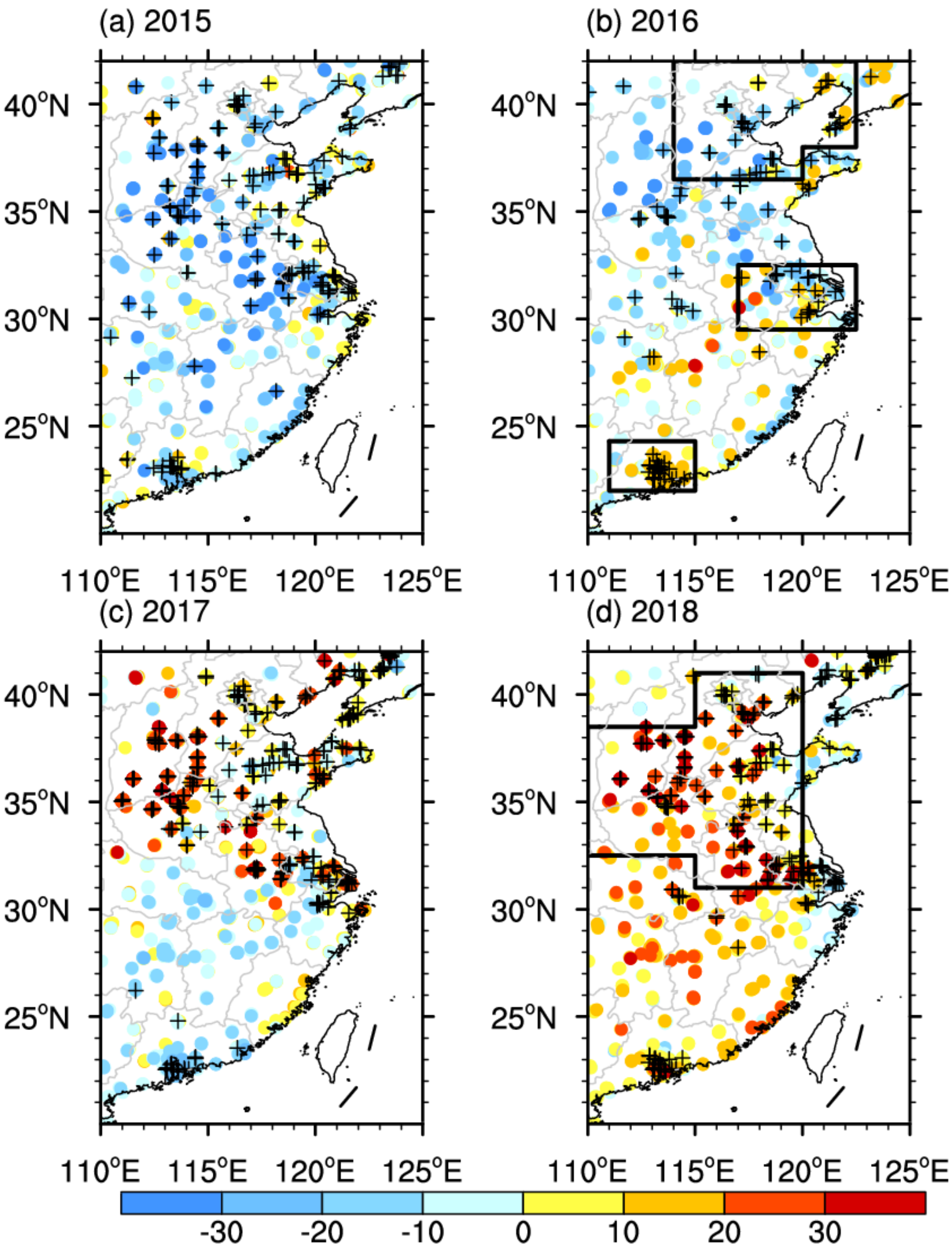

Figure 2. Anomalies of the summer mean MDA8 (Unit: μg/m³) in 2015 (a), 2016 (b), 2017 (c) and 2018 (d), relative to the mean during 2015–2018. The black pluses indicate that the maximum MDA8 was larger than 265 μg/m³. The black boxes in panel b indicated the locations of NC, YRD and PRD, while that in panel d was the NCH area.

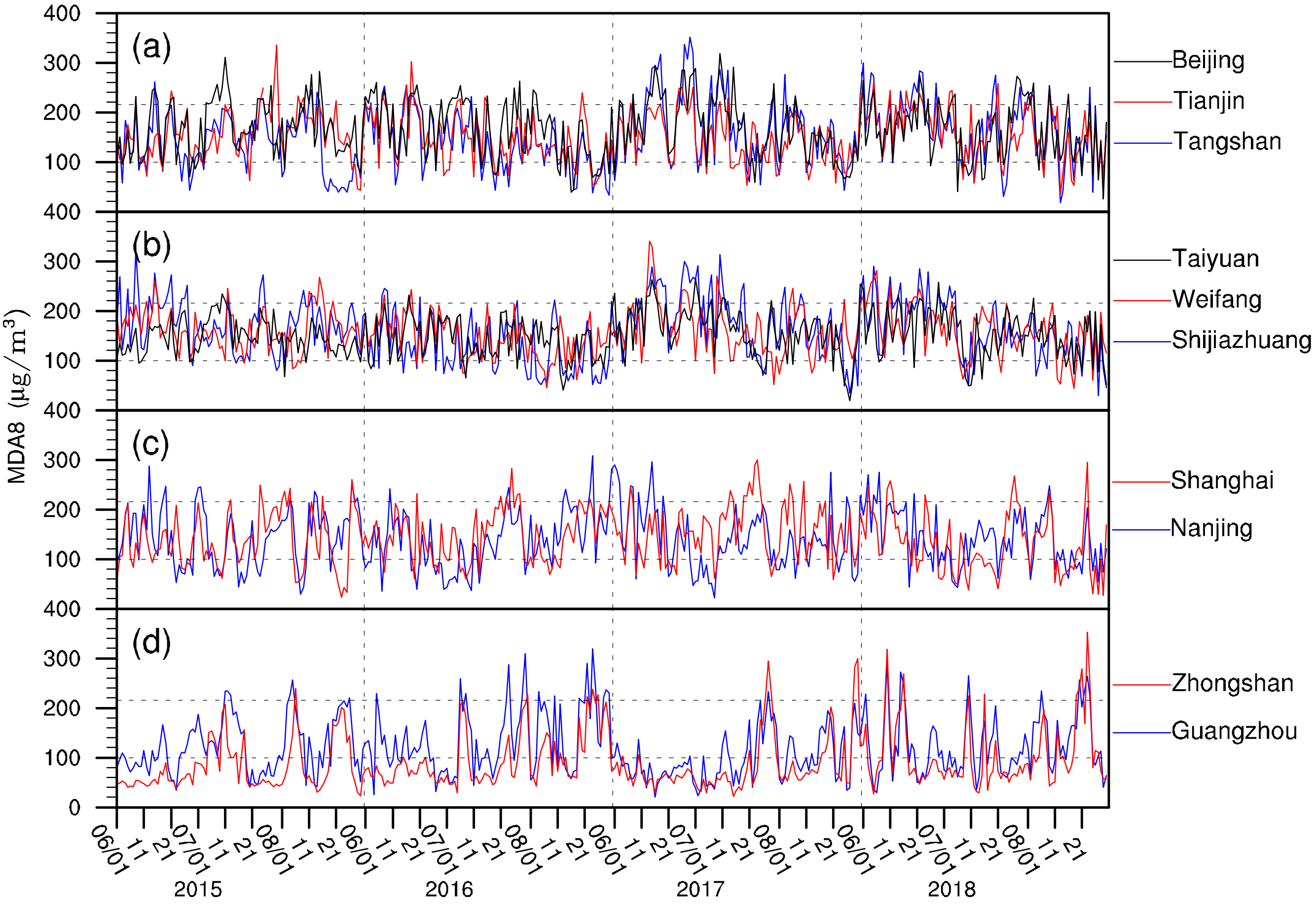

Figure 3. Variations in MDA8 (Unit: μg/m³) of polluted cities from 2015 to 2018, including (a) Beijing (capital of China), Tianjin and Tangshan near the capital city; (b) Taiyuan, Weifang and Shijiazhuang in the south of NCH; (c) Shanghai and Nanjing in YRD; and (d) Zhongshan and Guangzhou in PRD. The cities in panels (a)-(d) were located from north to south and were illustrated in Figure S2. The horizontal dash lines indicated the value of 100 μg/m³ and 215 μg/m³, and the vertical ones separated the years..

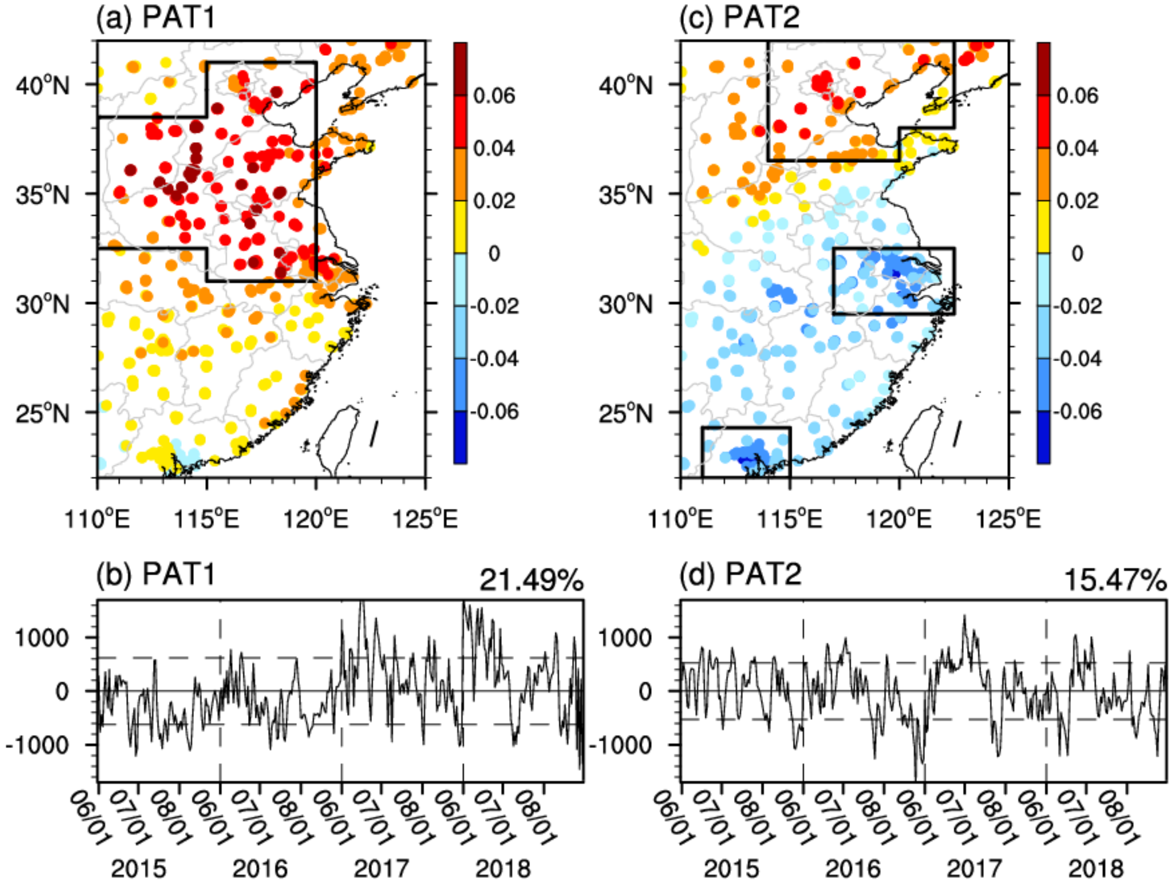

Figure 4. The first EOF pattern (PAT1: a, b) and second EOF pattern (PAT2: c, d) of MDA8 in summer from 2015 to 2018, including the spatial pattern (a, c) and the time coefficient (b, d). The black boxes in panels a and c are the selected NCH, NC, YRD and PRD. The EOF analysis were applied to the daily MDA8 anomalies at 868 stations to extract the relatively change 445 features of the original data on the daily time-scale. The percentages on panel (b) and (d) were the variance contributions of the first and second EOF mode. The horizontal dash lines indicated one standard deviation, and the vertical ones separated the years.

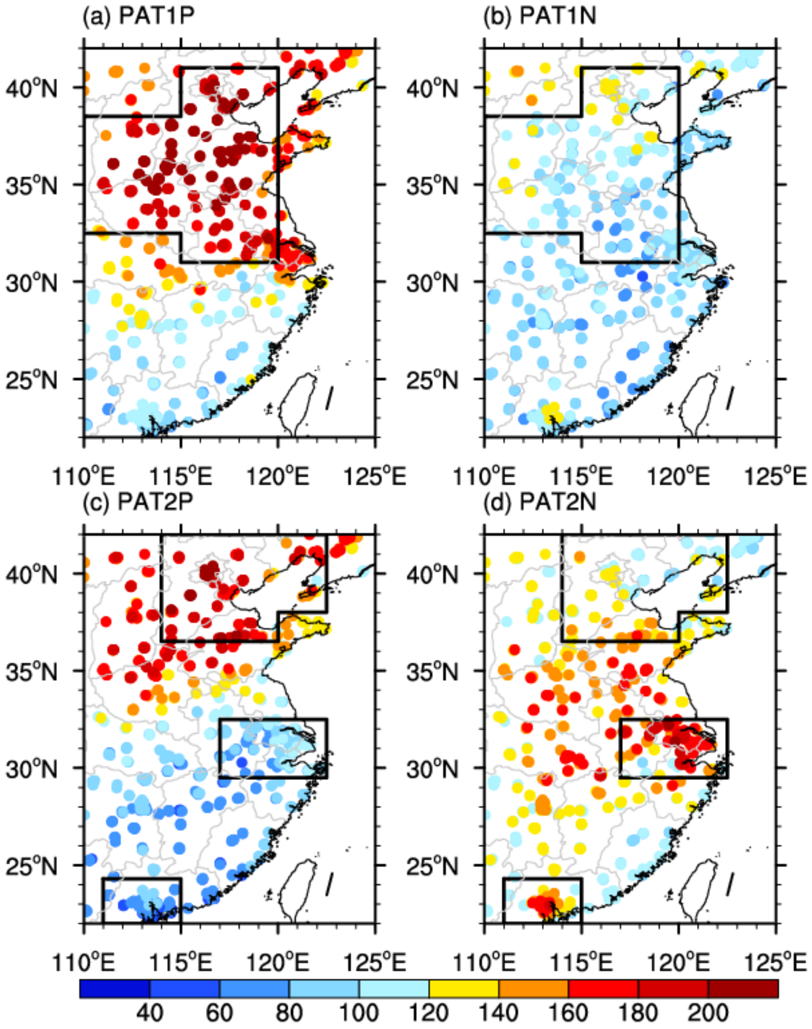

450 **Figure 5.** Composites of the MDA8 (Unit: μg/m³) for PAT1 (a, b) and PAT2 (c, d) in summer from 2015 to 2018. Panels (a) and (c) were composited when the time coefficient of EOF1 and EOF2 was greater than one standard deviation, while panels (b) and (d) were composited when the time coefficient was less than –1 ×one standard deviation. The black box in panel a-b indicated the location of NCH, while those in panel c-d were the NH, YRD and PRD area.

455

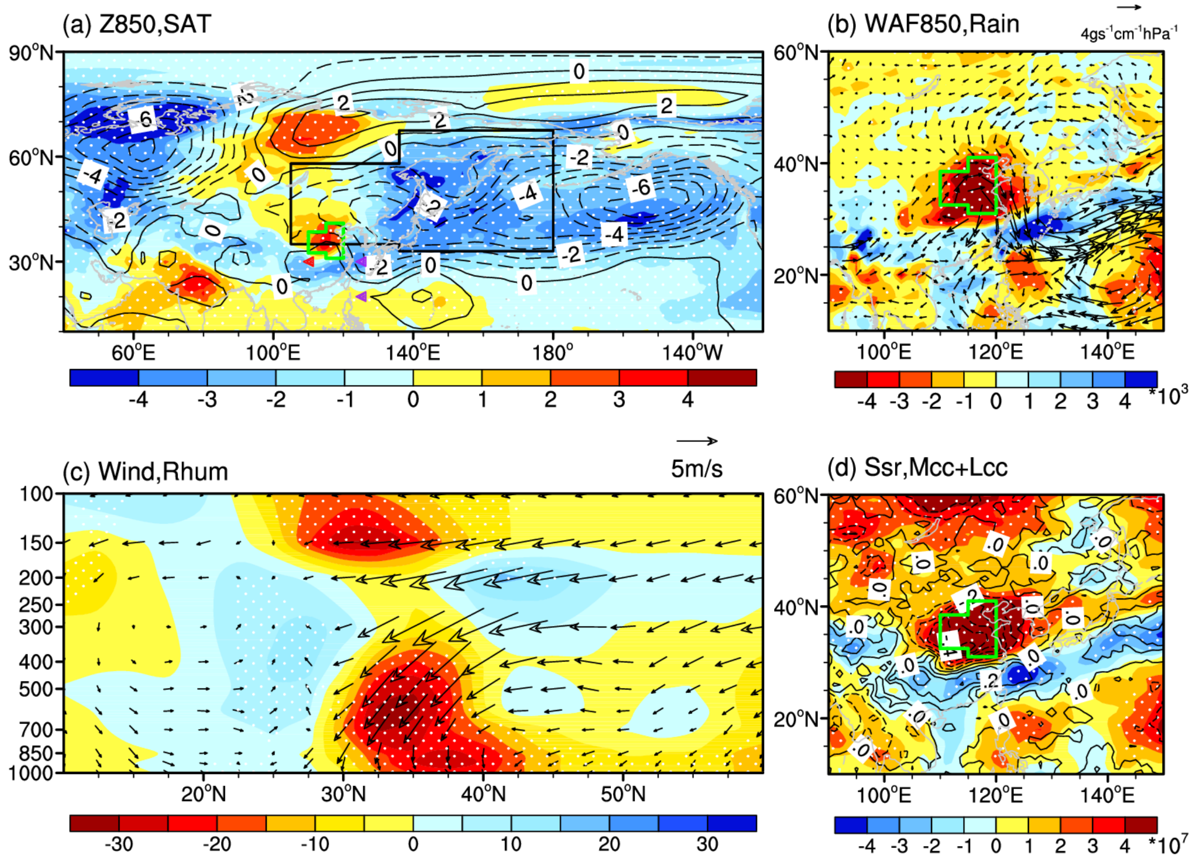

Figure 6. Differences of the daytime atmospheric circulations (i.e., PAT1P minus PAT1N). (a) Geopotential height at 850 hPa (Unit: 10gpm, contours) and surface air temperature (Unit: K, shading), (b) water vapor flux (Unit: 4×10^3 $gs^{-1}cm^{-1}hpa^{-1}$) at 850 hPa (arrows) and precipitation (Unit: mm, shading), (c) 100°E–120°E mean wind (Unit: m/s, arrows) and relative humidity (Unit: %, shading), (d) downward solar radiation at the surface (Unit:10^7 J/m^2, shading) and the sum of low and medium cloud cover (Unit: 1, contours). The white dots indicate that the shading was above the 95% confidence level. The green boxes in panels (a), (b) and (d) show the NCH region, and the black box in panel (a) indicates the location of the East Asia trough. The purple triangles in panel (a) indicated the data used to calculate the $WPSH_1$, while the red triangle represented the west ridge point of WPSH.

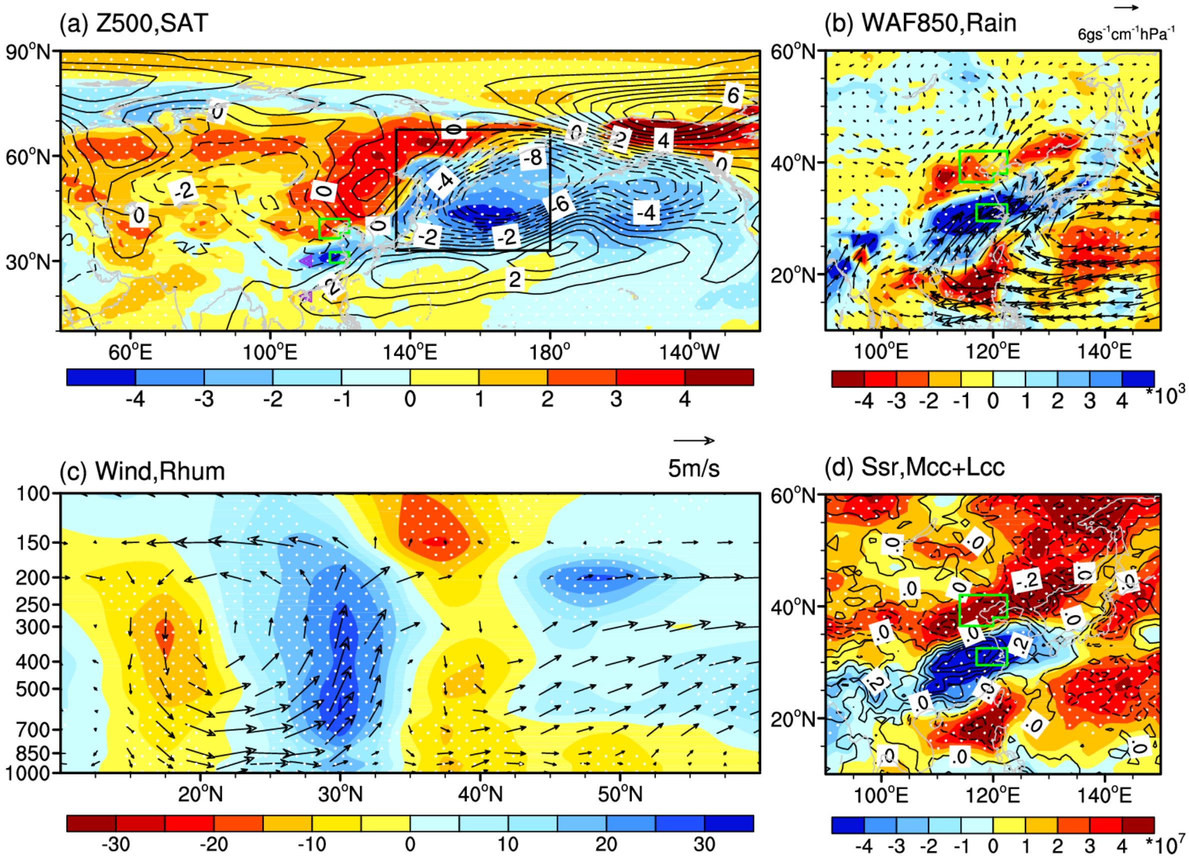

Figure 7. Differences of the daytime atmospheric circulations (i.e., PAT2P minus PAT2N). (a) Geopotential height at 500 hPa (Unit: 10gpm, contours) and surface air temperature (Unit: K, shading), (b) water vapor flux (Unit: 6×10^3 $gs^{-1}cm^{-1}hpa^{-1}$) at 850 hPa (arrows) and precipitation (Unit: mm, shading), (c) 100°E–120°E mean wind (Unit: m/s, arrows) and relative humidity (Unit: %, shading), (d) downward solar radiation at the surface (Unit: $10^7 J/m^2$, shading) and the sum of low and medium cloud cover (Unit: 1, contours). The white dots indicate that the shading was above the 95% confidence level. The green boxes in panel (a), (b) and (d) are the NC and YRD regions, and the black box in panel (a) indicates the location of the East Asia trough. The purple triangles in panel (a) indicated the data used to calculate the $WPSH_2$.

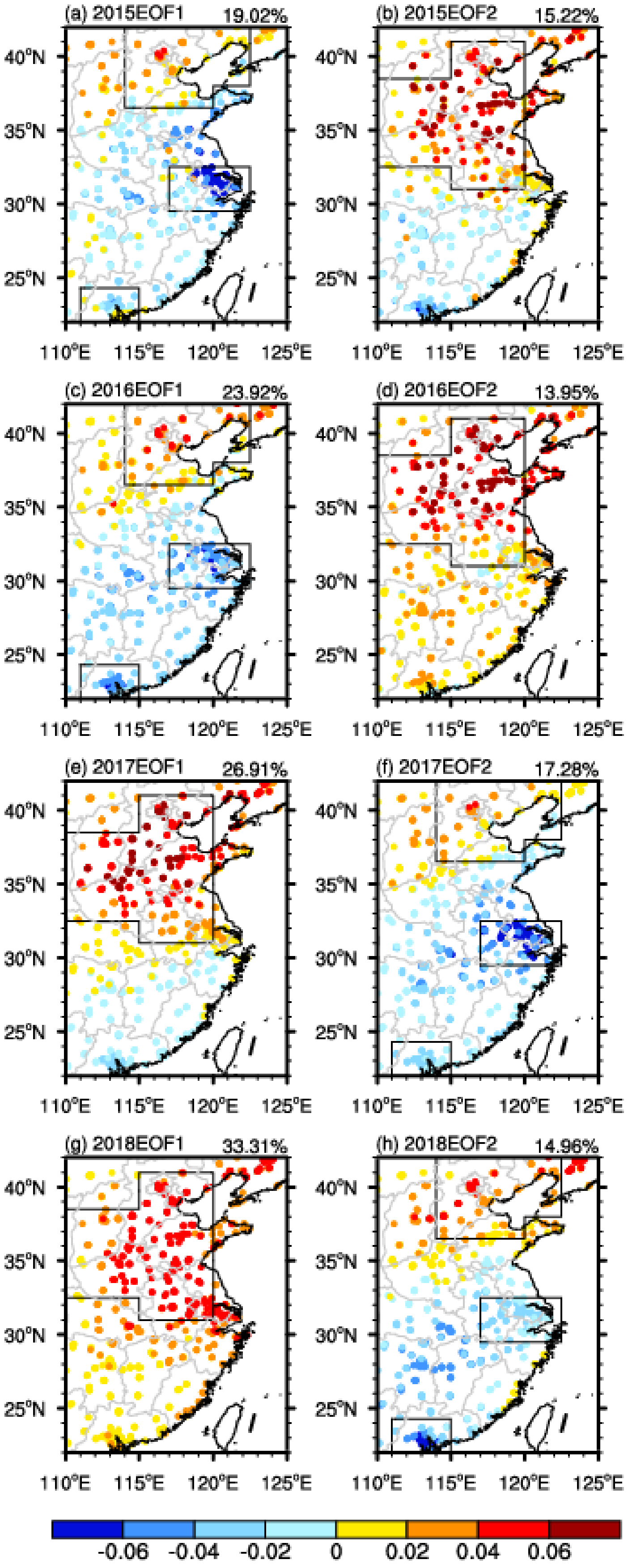

Figure 8. The first (a, c, e, g) and second (b, d, f, h) EOF spatial patterns of MDA8 in summer in 2015 (a, b), 2016 (c, d), 2017, (e, f) and 2018(g, h). The percentage number in panels (a, c, e, g) and (b, d, f, h) are the variance contributions of the first and second EOF mode. The black boxes indicated the location of NCH, NH, YRD and PRD, respectively.

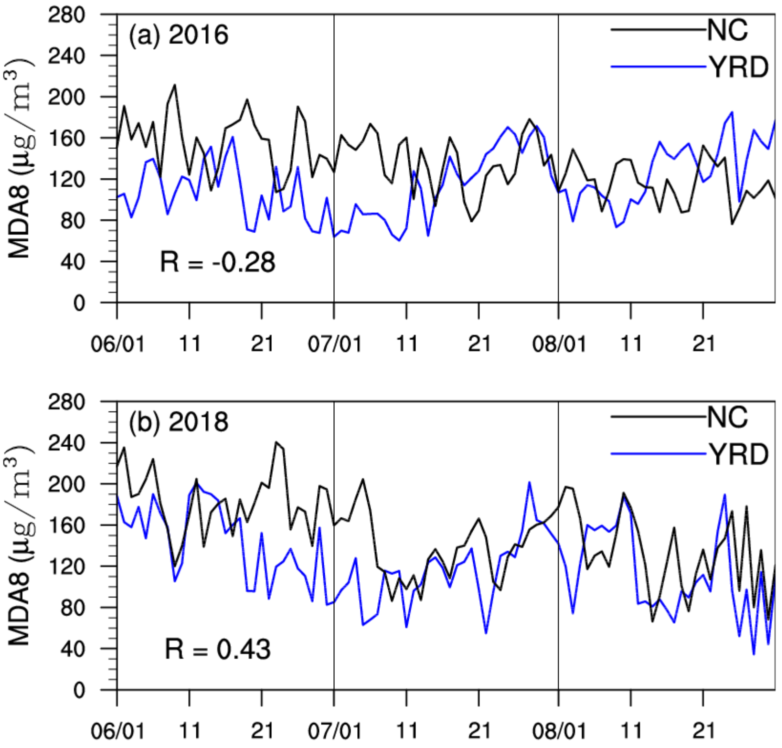

Figure 9. Variations in the MDA8 (Unit: μg/m³) of NC (black) and the YRD (blue) in 2016 (a) and 2018 (b). The MDA8 was calculated as an average for all available sites in the NC and the YRD regions.